

Towards Optical Biopsy of Olfactory Cells using Concentric Tube Robots with Follow-the-Leader Deployment

Cédric Girerd¹, Kanty Rabenorosoa², Patrick Rougeot² and Pierre Renaud¹

Abstract—In this paper, we propose to take advantage of concentric tube robots (CTR) properties to design a robotic system for optical biopsies with fiber-based imaging modalities. Follow-the-leader (FTL) deployment, with CTR body following its tip, is being integrated as a design constraint in order to minimize the device invasiveness. A design procedure is proposed and developed in the context of olfactory cell inspection. Stability issues of CTR are considered with theoretical validation of FTL deployment. Finally, an experimental assessment in lab conditions is being conducted that includes the device deployment and the reproduction of scanning task for imaging. The whole surface to be inspected can be accessed, and 20 μm resolution of the CTR tip is observed.

I. INTRODUCTION

Age-related neurodegenerative diseases have become one of the top priorities for health authorities worldwide [1], [2], [3]. Efficient treatment strategies are needed, and first of all diagnostic tools. Several recent clinical studies have demonstrated the existence of a correlation between the appearance of these pathologies and the loss of smell [4], [5], [6]. The neuropathologic changes of olfactory dysfunction in neurodegenerative diseases may involve the olfactory epithelium and olfactory bulb [7]. Inspection of these anatomical structures could therefore be the key for a new diagnostic approach. The validation of this assumption is however yet to be confirmed. This means a tool is needed to inspect *in vivo* the olfactory cells in research protocols.

There is today a growing number of optical techniques that could be considered for visualization of the olfactory cells. The size of these cells is in the order of a hundred micrometers. OCT (Optical Coherence Tomography) [8], confocal microscopy [9], and photo-acoustic imaging [10] are then of great interest, with the possibility to perform what can be described as an optical biopsy in order to reveal the anatomical structure. To the best of our knowledge, there is however today no tool to give access to the aforementioned anatomical areas. The anatomical constraints are indeed very strong, with an access that is possible only through the so-called olfactory clefts, located in the upper part of the nasal cavity, of complex shape and less than 2 mm in width. Even though an optical technique such as OCT can be based on the use of a single optical fiber, there is today no device to access to the olfactory cells and to perform an optical biopsy.

A robot-assisted optical biopsy can be of great interest, for the accuracy and repeatability generally obtained with a robotized approach [11]. Concentric tube robots (CTR) seem particularly well adapted [12]. The absence of actuator within the robot body allows the design of catheter-like structures with millimeter-size diameter. Furthermore, their design based on tubular structures in interaction allows the creation of continuum robots of hollow shape, compatible with the insertion of an optical fiber for optical biopsy. The achievable size of CTR make them suitable for navigation in complex environments. It has been therefore considered in several contexts, such as cardiac surgery [13], ENT surgery [14], [15], or intracerebral hemorrhage evacuation [16]. The tip of the CTR is then controlled by the modification of the relative position of the different superelastic and precurved tubes composing the robot. The tubes are in interaction, with bending and torsion effects. Thus, the use of CTR is hampered by two issues. First, the tube interactions can lead to instabilities, with a sudden release of the energy stored in the tubes known as a snapping effect [17]. Second, the control of the CTR tip usually also affects the shape of the CTR, and it limits its use in very narrow environments such as the one considered here.

The latter issue has been the object of an active research, with proposition of so-called follow-the-leader (FTL) deployment. The volume occupied by the CTR during its deployment is then minimal, since the robot body follows the path traced by its distal tip. Several conditions on the tube geometries have been introduced as well as deployment sequences [18], [19]. No detailed design method however exists for the design of a CTR for FTL deployment, and few works have indeed shown the potential of CTR with FTL deployment for solving all requirements related to a medical task. In this paper, we propose to evaluate the exact interest of CTR controlled with FTL deployment for an optical biopsy task. Three aspects are covered. First, a synthesis procedure of the CTR is presented. A simple method is introduced with decoupling between path determination and robot synthesis. It is associated to an experimental evaluation of the achievable accuracy of the FTL deployment. Second, the stability during deployment is assessed. The impact of transmission lengths, the CTR tube lengths required to the device actuation, is analyzed theoretically and experimentally, demonstrating the possibility to access olfactory cells safely. Third, scanning as required during an optical biopsy is experimentally evaluated.

The structure of the paper is as follows. In section II, the exact task requirements are described which lead to

¹Cédric Girerd and Pierre Renaud are with ICube, UDS-CNRS-INSa, 300 bd Sébastien Brant - Illkirch, France cedric.girerd@insa-strasbourg.fr

²Kanty Rabenorosoa and Patrick Rougeot are with FEMTO-ST institute, Univ. Bourgogne Franche-Comté, CNRS, Besançon, France rkanty@femto-st.fr

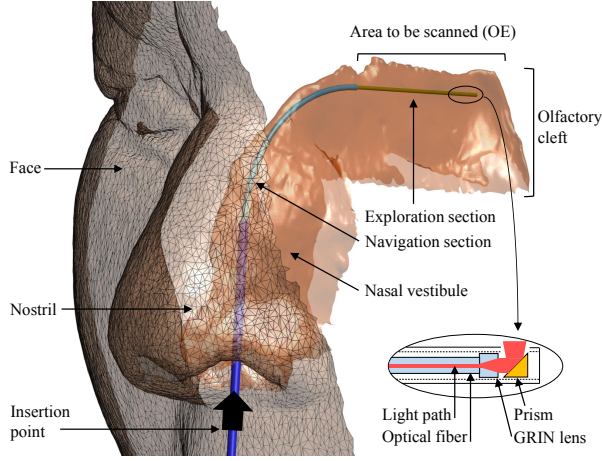


Fig. 1: CAD view of the proposed concentric tube robot after deployment in the nasal cavity for optical biopsy of the olfactory cells by OCT.

the generation of compatible paths, used later in the design process for the synthesis of the device. The CTR synthesis issue is addressed in section III in the particular context of FTL deployment, including verification of stability during deployment. Then, the experimental evaluation of FTL deployment and scanning for optical biopsy are presented in section IV. Conclusions and perspectives are summed up in section V.

II. TASK ANALYSIS FOR PATH GENERATION

A. Anatomical Constraints

Little information exists in the literature concerning the size and geometry of the nasal cavity, especially for the olfactory cleft. As a consequence, task analysis is based on a 3D reconstruction of the nasal cavity. The reconstructed volume is visible in Fig. 1. It is obtained from a dataset of 84 transverse images, equally spaced by 1 mm, with a resolution of $0.39 \text{ mm} \times 0.39 \text{ mm}$. The device insertion can be performed through the nostril, a flexible area appearing in the lower part of the nasal cavity. The nostril gives access to a thin and geometrically complex volume called the nasal vestibule that leads to the olfactory cleft, located in the upper part of the nose. The upper part of the olfactory cleft, the area to be inspected, is covered by the olfactory epithelium (OE), a thin and very fragile mucosa [20]. Given the shape of the nasal cavity, the synthesis of the robot can not be performed on 2D images. 3D reconstructions are required for the device synthesis. It however appears that the CTR diameter must not exceed 2 mm, with a curvilinear length of approximately 90 mm to scan the OE.

B. Task Requirements and Device Decomposition

The device is aimed at first reaching the entry of the olfactory cleft, after deployment from the nostril, and then scanning the roof of the olfactory cleft with a distal movement of the robot. Given the shape of the nostril, the entry point is not unique, and the pose of the CTR base can be

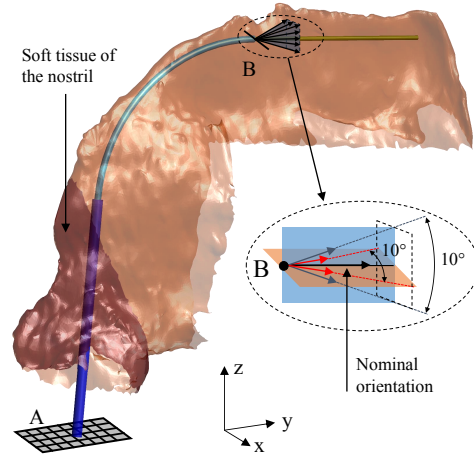


Fig. 2: Representation of the nasal cavity with task requirements: the CTR must start from area A to reach point B, with admissible distal orientations as represented in the close-up figure.

adjusted with respect to the nostril to reach successfully the olfactory cleft, as schematically represented in Fig. 2. Thus, the point A lies in a xy plane, defined parallel to the palate which is the base of the nasal cavity, and represents admissible entry points.

OCT seems today the most adequate imaging technique for the desired optical biopsy of the OE. Given the available space around the olfactory cleft, the only admissible configuration is to have the optical fiber for imaging approximately parallel to the area of interest, with a prism at the distal end of the robot to orientate the light rays on the area to be scanned (Fig. 1). Tolerance in the fiber/cleft angle is estimated equal to 10° as represented in B in Fig. 2. Distance between the cleft roof and the fiber must be equal to 3 mm, ± 1 mm, the working distance considered for the OCT probe to image the area [21], in the z direction. For integration reasons, an outer diameter of 0.6 mm of the optical fiber with the embedded prism is considered. Each acquisition with the OCT probe requires a lateral resolution about $15 \mu\text{m}$ in order to obtain high resolution images.

It appears clearly that the robotic task is the combination of two subtasks with different requirements. In a first step, we wish to deploy the CTR to reach the area of interest. The complexity of the path shape is here the main requirement, with FTL deployment to minimize the risks of unwanted contacts with the mucosa. We propose here to follow the functional decoupling introduced in [19], with the design of a navigation section solely for that subtask. In a second step, optical biopsy will be performed by distal motions of the CTR tip, using an exploration section. During that phase, the resolution of the tip movements is the main constraint.

C. Path generation and selection

The simplest way to ensure FTL deployment is to use constant-curvature tubes arranged in a plane to make a planar robot made of constant-curvature links [18], [19]. The

number of tubes of the CTR is then equal to the number of constant-curvature segments along the path, and the synthesis problem consists first to determine a path that is compatible with all the task requirements described in section II.B. A path is defined by

- 1) the number of constant-curvature segments,
- 2) the curvature values,
- 3) the position of the path proximal end,
- 4) the distance between the distal path end and the roof of the olfactory cleft,
- 5) the orientation of the tangent vector to the path at the distal end with respect to the roof of the olfactory cleft, as described in Fig. 2.

Today, ENT surgeons can access the upper part of the nasal vestibule using straight tools. As a consequence, the proximal segment of the path is chosen straight. Similarly, given the shape of the olfactory cleft, a straight segment is considered for the distal section, which will be the exploration section. From a visual examination of the anatomy, a single curved segment is considered to connect the other two segments, whose curvature has to be determined.

A path is admissible if no collision is observed between the associated robot shape and the nasal cavity, after suppression of the soft tissue of the nostril. Admissible paths require a collision evaluation that is therefore performed for all possible paths obtained after definition and discretization of intervals for the curvature of the middle segment and the properties 3), 4) and 5) defined above. For collision detection, using the V-Collide library [22], volumes need to be defined from the path segments. Cylindrical shapes are considered. Outer diameters are selected from standard dimensions of tubes as available at Euroflex GmbH (Pforzheim, Germany). The diameter of the distal segment is chosen taking into account the internal diameter needed for the optical fiber, the prism and the required GRIN lens. Diameters are defined equal to 1.6, 1.0 and 0.65 mm starting from the nostril.

Three different possible curvatures for the second segment are identified, with values of 0.03, 0.04 and 0.05 mm⁻¹. The result can obviously depend on the subject anatomy. The presented methodology has been therefore applied on 19 subject reconstructions obtained in [23], and the curvature of 0.04 mm⁻¹ is admissible for 42% of inspections, which is sufficient for the intended research protocol. For the anatomy presented in Fig. 1, 25 paths are identified for this value of curvature. The curvatures γ_i , $i \in [1,3]$, as well as the minimal and maximal values of the lengths l_i for the 25 paths $l_{i \min}$ and $l_{i \max}$ of the path segments, are summed up in Table I.

TABLE I: Path segment definitions. For the lengths, the minimum and maximum values obtained over the 25 admissible paths are reported.

| Segment index i | 1 | 2 | 3 |
|--------------------------------|-------|-------|-------|
| γ_i (mm ⁻¹) | 0.00 | 0.04 | 0.00 |
| $l_{i \min}$ (mm) | 34.94 | 32.55 | 27.00 |
| $l_{i \max}$ (mm) | 40.35 | 37.76 | 27.00 |

III. CTR SYNTHESIS

For FTL deployment, the CTR is here necessarily composed of 3 tubes. Let i be the tube index number, with $i=1$ for the inner tube. The tubes, of lengths L_i , $i \in [1,3]$ are deployed out of the insertion point represented in Fig. 1, defined by the curvilinear abscissa $s = 0$. Some part of the tubes are necessary for the actuation, with the tubes individually uncovered to be attached to an actuation unit. These tube portions are called transmission lengths, and denoted by lengths β_i , $i \in [1,3]$. During deployment, the link lengths of the robot are denoted l_{li} , with $0 \leq l_{li} \leq L_i$.

A. Follow-The-Leader Deployment

The deployment sequence for FTL is illustrated in Fig. 3, following [18], [19]. The first step consists in deploying all tubes altogether, with alignment of their distal ends. Tube 3 is stopped when the end of the first segment on the path is reached. Afterwards, only the two inner tubes are deployed, keeping their distal ends aligned. Finally, when tube 2 reached the end of the second segment, tube 1 continues his deployment for the exploration task. The maximum deployed lengths for tube 3, 2 and 1 are respectively l_1 , $l_1 + l_2$ and $l_1 + l_2 + l_3$ (see Table III). From the sequence, the sum of the tube lengths and transmission lengths $L_i + \beta_i$, $i \in [1,3]$ can be expressed at any time as given in Table II.

B. Tube geometries

The proximal path segment is of straight shape. As a consequence, only small curvature changes will occur for tube 3. A simple stainless steel is then being used for the outer tube (Phynox, Young's modulus: 203 Gpa, Poisson's ratio: 0.30). The two internal tubes are made out of Nitinol

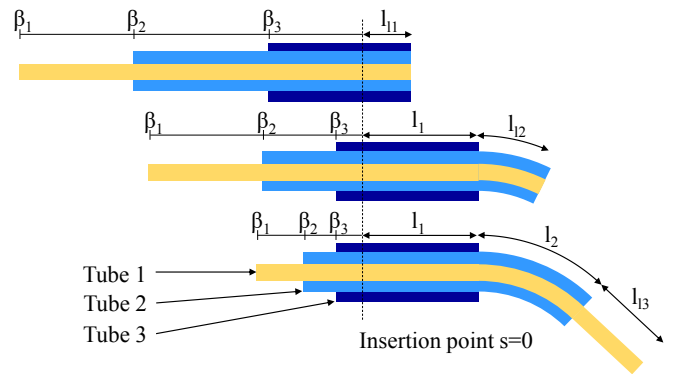


Fig. 3: FTL deployment. On top, the first step, in the middle the second step and at the bottom the third insertion step.

TABLE II: Values of the deployed lengths during deployment, as functions of the path lengths (l_1, l_2, l_3) and the link lengths (l_{l1}, l_{l2}, l_{l3}).

| Deployed length | Step 1 | Step 2 | Step 3 |
|-----------------|----------|----------------|----------------------|
| $L_1 + \beta_1$ | l_{l1} | $l_1 + l_{l2}$ | $l_1 + l_2 + l_{l3}$ |
| $L_2 + \beta_2$ | l_{l1} | $l_1 + l_{l2}$ | $l_1 + l_2$ |
| $L_3 + \beta_3$ | l_{l1} | l_1 | l_1 |

TABLE III: CTR geometry after synthesis

| Tube index | Inner diam. (mm) | Outer diam. (mm) | Curvature mm ⁻¹ | Deployed length (mm) | L_i (mm) |
|------------|------------------|------------------|----------------------------|----------------------|------------|
| 1 | 0.610 | 0.650 | 0.0000 | 99.90 | 300.0 |
| 2 | 0.770 | 1.010 | 0.0423 | 72.90 | 143.0 |
| 3 | 1.100 | 1.600 | 0.0021 | 40.35 | 60.4 |

for the provided superelasticity (Young's modulus: 80 GPa, Poisson's ratio: 0.33). The dimensions of tube 1 and 2 are chosen as standard dimensions, as detailed in section II.C. The bending stiffnesses of the tubes k_{bi} , $i \in [1, 3]$ can then be computed. From these properties, it is possible to determine the tube curvatures κ_i , $i \in [1, 3]$ following the expressions we developed in [24]:

$$\kappa_1 = \gamma_n \quad \text{and} \quad \kappa_{j,j>1} = \frac{1}{k_{bj}} \left(\sum_{i=1}^j k_{bi} \gamma_{n+1-j} - \sum_{i=1}^{j-1} k_{bi} \kappa_i \right) \quad (1)$$

The obtained parameters describing the tube geometries are reported in Table III. The designed CTR is thus composed of 3 links, the first one containing a straight tube and two curved tubes with opposite curvatures, a second link with a straight and a curved tube, and a third link with only a straight tube. Among the 25 possible paths, the one with the longest first section is then considered. Given the deployment sequence, this is the most difficult scenario and then a worst-case situation, since in that section the 3 tubes are in interaction, which can lead to instabilities, analyzed hereafter.

C. Stability Assessment

During the deployment, the CTR tubes are arranged in a planar configuration. The CTR can then be considered as a 3-link robot, with link lengths l_{li} , $i \in [1, 3]$ varying during the deployment as represented in Fig. 3. The tube curvatures are either aligned or in opposition, this latter case being possibly unstable [25], [26]. In our case, tube 2 and 3 have opposite curvatures, and tube 1 can be in any angular position, as it is straight. The transmission lengths play then an important role in the robot stability, and as such must be considered. Several recent results have been introduced for evaluating the stability of a CTR in the general case [25], [26], [27]. The approach developed in [25] is interesting as it is an analytic approach based on the computation of a matrix designated as \mathbf{W}_2 , that represents the moment-free boundary condition at the robot tip. Stable robot configurations are characterized by $\det(\mathbf{W}_2) > 0$.

Using the criteria from [25], $\det(\mathbf{W}_2)$ can here be expressed as a function of the deployed length l_{l1} of CTR link 1, κ_i , k_{bi} , k_{ti} and β_i respectively the curvature, bending and torsional stiffnesses, and the transmission length of tube i . The values of l_{l1} and β_i , $i \in [1, 3]$ vary during deployment.

$$\det(\mathbf{W}_2) = \cosh(l_{l1}\alpha) - \alpha \sinh(l_{l1}\alpha) \left(\frac{\beta_2 k_{3t} + \beta_3 k_{2t}}{k_{2t} + k_{3t}} \right) \quad (2)$$

with

$$\alpha = \sqrt{-\kappa_2 \kappa_3 \frac{k_{3b} k_{2b} (k_{2t} + k_{3t})}{(k_{1b} + k_{2b} + k_{3b}) k_{2t} k_{3t}}}$$

It is interesting to outline that the stability condition only depends on one link length, namely l_{l1} . Instability can appear if at least two tubes have opposite curvatures. For the section 2 of the path, only one curved tube is being used. Stability is therefore logically always obtained. For section 3 of the path, only one tube is involved. Once again, stability is therefore always obtained. The only instability can be linked to deployment along section 1, with two tubes of opposite curvatures that can cause instabilities. Also, the transmission length of the straight inner tube β_1 does not appear in the equation, and is therefore unconstrained. The robot is known to be stable in a given configuration if $\det(\mathbf{W}_2) > 0$. In order to assess the stability of the robot during deployment, the sign of $\det(\mathbf{W}_2)$ is studied as the robot is steered along segments lengths l_1 , l_2 and l_3 . During the first deployment step, as link 1 is being extended, we have the equalities listed in Table II, leading to the expression in (3).

$$\det(\mathbf{W}_2(l_{l1}))|_{\text{Step 1}} = \cosh(l_{l1}\alpha) - \alpha \sinh(l_{l1}\alpha) \left(\frac{(l_{l1} - L_2)k_{3t} + (l_{l1} - L_3)k_{2t}}{k_{2t} + k_{3t}} \right) \quad (3)$$

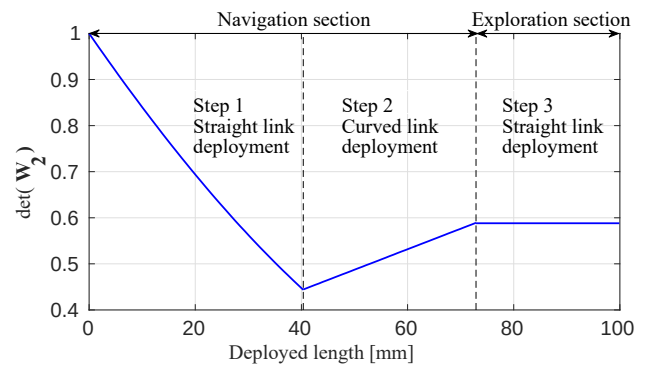
Then, during the step 2, as link 2 is being extended, we have

$$\det(\mathbf{W}_2(l_{l2}))|_{\text{Step 2}} = \cosh(l_1\alpha) - \alpha \sinh(l_1\alpha) \left(\frac{(l_1 + l_{l2} - L_2)k_{3t} + (l_1 - L_3)k_{2t}}{k_{2t} + k_{3t}} \right) \quad (4)$$

Finally, during step 3, we obtain a constant value for the expression of the determinant:

$$\det(\mathbf{W}_2(l_{l3}))|_{\text{Step 3}} = \cosh(l_1\alpha) - \alpha \sinh(l_1\alpha) \left(\frac{(l_1 + l_2 - L_2)k_{3t} + (l_1 - L_3)k_{2t}}{k_{2t} + k_{3t}} \right) \quad (5)$$

Fig. 4 represents the value of $\det(\mathbf{W}_2)$ as a function of the deployed length. The determinant value is always positive, which means that the robot does not undergo any bifurcation, which means an exact FTL deployment can be performed. Moreover, we have shown that the deployment of tube 1

Fig. 4: Value of $\det(\mathbf{W}_2)$ during the FTL deployment

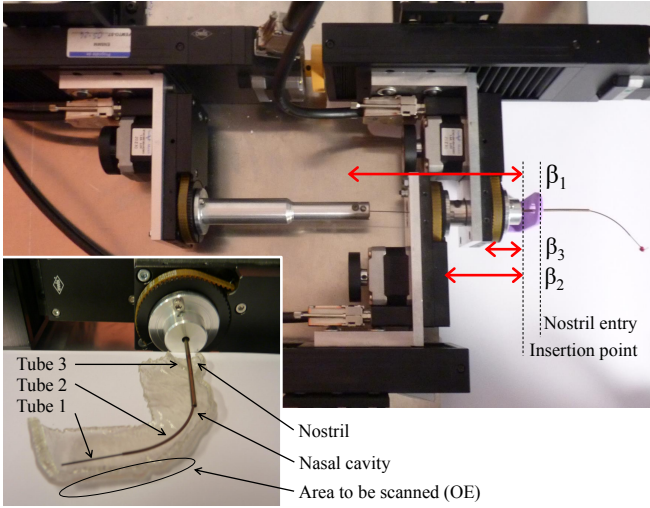


Fig. 5: Top: the actuation unit with the three tubes and a hollow part in violet to reproduce the insertion area. Bottom: Close-up after FTL deployment, with the CTR tip reaching the end of the olfactory cleft roof on a 3D-printed anatomical structure.

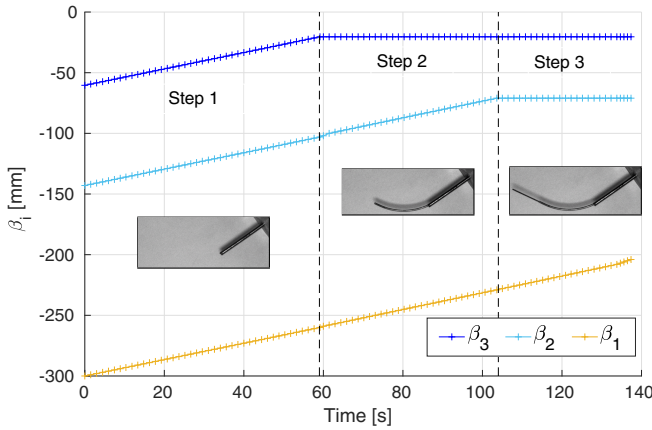


Fig. 6: Evolution of the actuator positions during the deployment with the CTR configurations represented at the end of each step. During deployment, we have $\beta_1 \in [-300 - 200]$, $\beta_2 \in [-143 - 70]$, $\beta_3 \in [-60.4 - 20]$

in the third section of the robot does not impact the robot stability, and this tube can have infinite transmission length. Its rotation does not impact the robot shape as it is straight, leading to perfect scanning performance in the absence of friction between the tubes.

IV. EXPERIMENTAL VALIDATION

A. Experimental Setup

An existing actuation unit is being used to assess the FTL deployment strategy and the scanning performance. It is based on 3 motorized linear stages (LIMES 90-55-HSM, stepper motor) and 3 motorized rotary stages (DRMT 65-D25-HSM, stepper motor) from OWIS (Staufen, Germany). Only the rotary stage linked to tube 1 is actuated, as the

other tubes are simply translated. It is controlled through a Matlab interface on a desktop computer (Dell, Intel Core 3.4GHz). For availability reasons, this first prototype is built using Nitinol tubes, with inner diameters of 0.610, 0.770 and 1.760 mm, and external diameters of 0.650, 1.070 and 2.180 mm for tubes 1, 2 and 3 respectively. The synthesis procedure is applied with this choice of material and diameters. Curvatures of tubes are then equal to 0.000, 0.042, and 0.003 mm^{-1} for tubes 1, 2 and 3 respectively. Stability assessment is similarly performed, which shows that a stable FTL deployment is ensured. Image acquisitions of the CTR shape and tip position are performed using Visual Servoing Platform (ViSP) using two IEEE 1394 Guppy FireWire camera to capture top and side views of the robot.

B. Experimental Results

1) *FTL deployment*: The deployment sequence detailed in Fig. 3 is being used with the CTR prototype. Please also refer to the video accompanying this publication for demonstration of CTR with follow-the-leader deployment validation. The reference path is chosen among the 25 admissible trajectories identified in section II. Fig. 6 shows the corresponding recorded variations of β_1 , β_2 , β_3 . For evaluation of the CTR configuration after deployment, one half of the anatomical structure is 3D-printed and positioned below the CTR. This allows to see the CTR position, and its final configuration appears satisfactory with respect to the roof of the olfactory cleft, as it can be seen from Fig. 5.

Quantitative measurements are then achieved to evaluate the accuracy of the FTL deployment and existing deviations between the CTR tip trace and the path of the robot body. To do so, a vision-based measurement is performed. Visual

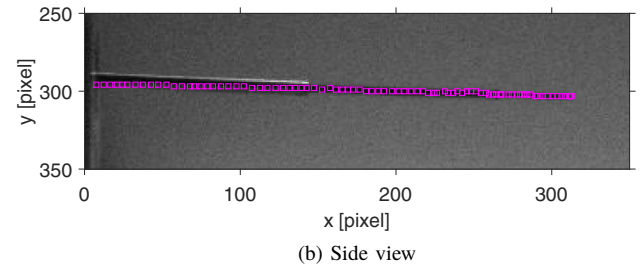
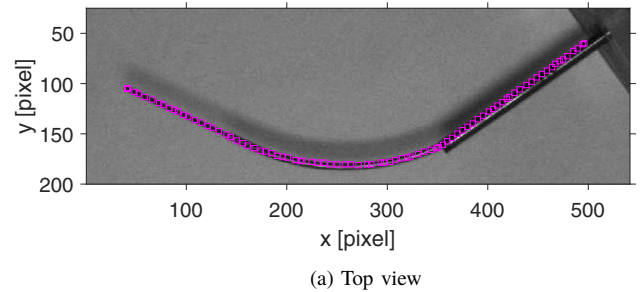


Fig. 7: Comparison of CTR tip trace and final CTR shape after deployment.

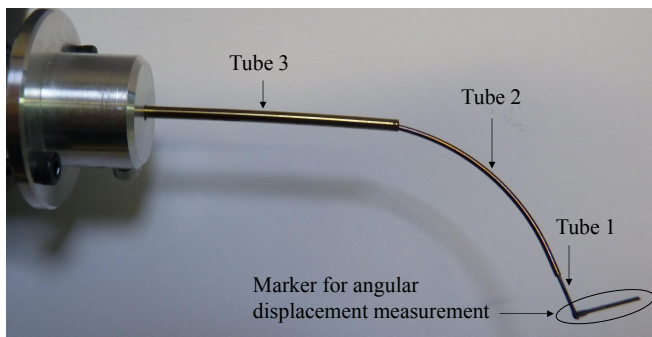


Fig. 8: Setup for the measurement of the tip self-rotation during scanning.

tracking of the CTR tip during deployment is performed using a normalized cross correlation technique [28]. The distances in the images (Fig. 7a and 7b) between the robot body after deployment and successive tip positions are estimated to finally compute the RMS values along the path segments.

The RMS value along the whole deployment for the top view is equal to 0.90 mm, and 0.18 mm for the side view. This means that the area to be scanned is successfully reached, with an accuracy in the FTL deployment that is satisfactory with respect to the task requirements.

2) *Scanning performance*: The scanning phase is performed using the translation and rotation of tube 1. Two characteristics need to be assessed, given the presence of friction between the tubes and its possible impact of the CTR behavior. First, the ability to scan the whole roof of the olfactory cleft, using the combination of these translation and rotation, needs to be verified. Second, the resolution in translation during the scanning step has to be verified in order to be able to gather OCT measurements.

The first set of experiments is performed after addition of a section of tube in a vertical position on the tube 1 as shown in Fig. 8. The angle of the distal end of tube 1 can then be extracted using a vision-based measurement. Translation steps of 0.5 mm and rotations of 60° are applied at the base

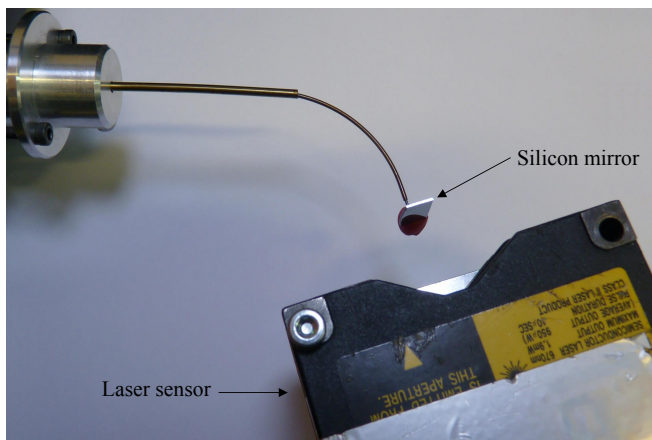


Fig. 9: Setup for the measurement of the displacement of the distal part of tube 1 during scanning phase.

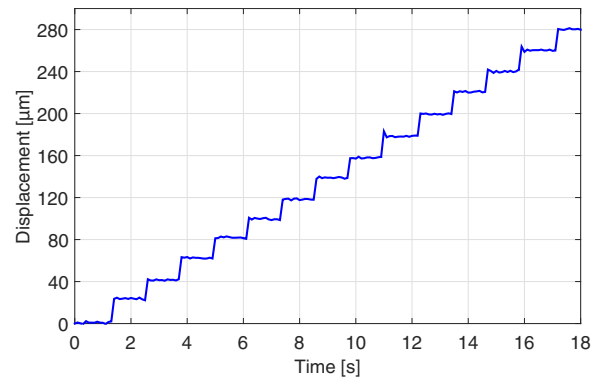


Fig. 10: Measurement of the CTR tip position during translation steps of 20 μm controlled at the proximal end of tube 1.

of tube 1. Measurements of the distal end angle show that a rotation of 34.5° can be obtained, and after several steps the length of the olfactory cleft, in the order of 25 mm, can be covered. Given the width of the olfactory cleft roof, a rotation of approximately 20° is sufficient to fully cover the OE. In the end, the surface to inspect appears to be effectively accessed during the scanning phase. One can note that a significant difference exists between the angle at the base and at the end of tube 1. Such difference is due to the tube torsion, and it could be compensated in a future device after a calibration. It is more important to note that tube 1 is somehow difficult to translate, with a visible bending of proximal end of tube 1 during the scanning phase. Such bending effect is due to its low bending stiffness and the presence of friction between tube 1 and the other tubes. This means the transmission length of tube 1 should be minimized to ensure correct deployment and scanning performances.

The second set of experiments aims at evaluating the resolution in translation of the CTR tip. The results are shown in Fig. 10 where one can observe the translational resolution at the distal end of tube 1, for translation step sizes of 20 μm of the actuator, its nominal resolution, at its proximal end. These values were acquired with a Keyence LC 2420 laser sensor in the direction of translation of tube 1 (Fig. 9). The amplitude of the step displacements is satisfactory, with 20 μm translations in average. This value remains a bit high for a continuous scanning with OCT, but this is linked to the resolution of the current actuation unit.

V. CONCLUSIONS

In this paper, we have proposed to use CTR with FTL deployment to perform new optical biopsy task of the olfactory cells. Using a 3D reconstruction of the anatomy, the CTR synthesis could be performed taking into account FTL constraints, with a design procedure that can be of interest in other medical contexts. One key issue for CTR is stability, taking into account the transmission lengths. We have here derived stability conditions for the 3-tube case and demonstrated in the medical context that this stability can

be ensured during FTL deployment. Experimental analysis in lab conditions confirms the satisfactory behavior. FTL deployment errors were measured with a RMS error of 0.9 mm, and the translational resolution that could be achieved for the scanning step was 20 μm . The experimental results outline the need for limiting transmission lengths in order to limit inner tube torsion. This aspect will now be investigated with design of a dedicated actuation unit, of better resolution for scanning and higher compactness also for compatibility with the medical context.

ACKNOWLEDGMENT

The authors would like to thank Guillaume Laurent for his support with the CVLink libraries. This work was supported by the French National Agency for Research within the Biomedical Innovation program (NEMRO ANR-14-CE17-0013), and the Investissements d'Avenir (Robotex ANR-10-EQPX-44, Labex CAMI ANR-11-LABX-0004 and Labex ACTION ANR-11-LABX-0001-01).

REFERENCES

- [1] C.-W. Hung, Y.-C. Chen, W.-L. Hsieh, S.-H. Chiou, and C.-L. Kao, "Ageing and neurodegenerative diseases," *Ageing research reviews*, vol. 9, pp. S36–S46, 2010.
- [2] P. S. Spencer, V. S. Palmer, and G. E. Kisby, "Seeking environmental causes of neurodegenerative disease and envisioning primary prevention," *NeuroToxicology*, vol. 56, pp. 269–283, 2016.
- [3] U. Sommer, T. Hummel, K. Cormann, A. Mueller, J. Frasnelli, J. Kropp, and H. Reichmann, "Detection of presymptomatic parkinson's disease: combining smell tests, transcranial sonography, and spect," *Movement disorders*, vol. 19, no. 10, pp. 1196–1202, 2004.
- [4] S. Rahayel, J. Frasnelli, and S. Joubert, "The effect of alzheimer's disease and parkinson's disease on olfaction: a meta-analysis," *Behavioural brain research*, vol. 231, no. 1, pp. 60–74, 2012.
- [5] L. Velayudhan, M. Pritchard, J. F. Powell, P. Proitsi, and S. Lovestone, "Smell identification function as a severity and progression marker in alzheimer's disease," *International Psychogeriatrics*, vol. 25, no. 07, pp. 1157–1166, 2013.
- [6] J. J. Stamps, L. M. Bartoshuk, and K. M. Heilman, "A brief olfactory test for alzheimer's disease," *Journal of the neurological sciences*, vol. 333, no. 1, pp. 19–24, 2013.
- [7] J. Attems, L. Walker, and K. A. Jellinger, "Olfactory bulb involvement in neurodegenerative diseases," *Acta neuropathologica*, vol. 127, no. 4, pp. 459–475, 2014.
- [8] R. A. McLaughlin, B. C. Quirk, A. Curatolo, R. W. Kirk, L. Scolaro, D. Lorensen, P. D. Robbins, B. A. Wood, C. M. Saunders, and D. D. Sampson, "Imaging of breast cancer with optical coherence tomography needle probes: feasibility and initial results," *IEEE Journal of Selected Topics in Quantum Electronics*, vol. 18, no. 3, pp. 1184–1191, 2012.
- [9] M. B. Wallace and P. Fockens, "Probe-based confocal laser endomicroscopy," *Gastroenterology*, vol. 136, no. 5, pp. 1509–1513, 2009.
- [10] S. Sethuraman, S. R. Aglyamov, J. H. Amirian, R. W. Smalling, and S. Y. Emelianov, "Intravascular photoacoustic imaging using an ivus imaging catheter," *IEEE transactions on ultrasonics, ferroelectrics, and frequency control*, vol. 54, no. 5, 2007.
- [11] R. H. Taylor, A. Menciassi, G. Fichtinger, and P. Dario, "Medical robotics and computer-integrated surgery," in *Springer handbook of robotics*. Springer, 2008, pp. 1199–1222.
- [12] H. B. Gilbert, D. C. Rucker, and R. J. Webster III, *Concentric Tube Robots: The State of the Art and Future Directions*. Cham: Springer International Publishing, 2016, pp. 253–269.
- [13] A. H. Gosline, N. V. Vasilyev, E. J. Butler, C. Folk, A. Cohen, R. Chen, N. Lang, P. J. Del Nido, and P. E. Dupont, "Percutaneous intracardiac beating-heart surgery using metal mems tissue approximation tools," *The International journal of robotics research*, 2012.
- [14] P. J. Swaney, H. B. Gilbert, R. J. Webster, P. T. Russell, and K. D. Weaver, "Endonasal skull base tumor removal using concentric tube continuum robots: a phantom study," *Journal of Neurological Surgery Part B: Skull Base*, vol. 76, no. 02, pp. 145–149, 2015.
- [15] L. Wu, S. Song, K. Wu, C. M. Lim, and H. Ren, "Development of a compact continuum tubular robotic system for nasopharyngeal biopsy," *Medical & biological engineering & computing*, pp. 1–15, 2016.
- [16] J. Burgner-Kahrs, D. C. Rucker, and H. Choset, "Continuum robots for medical applications: A survey," *IEEE Transactions on Robotics*, vol. 31, no. 6, pp. 1261–1280, 2015.
- [17] R. J. Webster III, J. M. Romano, and N. J. Cowan, "Mechanics of precurved-tube continuum robots," *IEEE Transactions on Robotics*, vol. 25, no. 1, pp. 67–78, 2009.
- [18] H. B. Gilbert, J. Neimat, and R. J. Webster, "Concentric tube robots as steerable needles: Achieving follow-the-leader deployment," *IEEE Transactions on Robotics*, vol. 31, no. 2, pp. 246–258, 2015.
- [19] C. Bergeles, A. Gosline, N. Vasilyev, P. Codd, P. del Nido, and P. Dupont, "Concentric tube robot design and optimization based on task and anatomical constraints," *IEEE Transactions on Robotics*, vol. 31, no. 1, pp. 67–84, Feb 2015.
- [20] A. L. Calof, N. Hagiwara, J. D. Holcomb, J. S. Mumm, and J. Shou, "Neurogenesis and cell death in olfactory epithelium," *Developmental Neurobiology*, vol. 30, no. 1, pp. 67–81, 1996.
- [21] Agiltron. (2012) Miniature oct fiber probe. [Online]. Available: <http://www.agiltron.com/PDFs/Miniature%20OCT%20Fiber%20Probe.pdf>
- [22] T. C. Hudson, M. C. Lin, J. Cohen, S. Gottschalk, and D. Manocha, "V-collide: Accelerated collision detection for vrml," in *Proceedings of the Second Symposium on Virtual Reality Modeling Language*, ser. VRML '97. New York, NY, USA: ACM, 1997, pp. 117–ff.
- [23] C. Girerd, K. Rabenorosoa, and P. Renaud, "Synthesis of a new concentric tube robot for olfactory cells exploration," in *CRAS: Computer/Robot Assisted Surgery*, 2016.
- [24] —, "Combining tube design and simple kinematic strategy for follow-the-leader deployment of concentric-tube robots," in *Advances in Robot Kinematics*, 2016.
- [25] H. B. Gilbert, R. J. Hendrick, and R. J. Webster III, "Elastic stability of concentric tube robots: a stability measure and design test," *IEEE Transactions on Robotics*, vol. 32, no. 1, pp. 20–35, 2016.
- [26] R. J. Hendrick, H. B. Gilbert, and R. J. Webster, "Designing snap-free concentric tube robots: A local bifurcation approach," in *Robotics and Automation (ICRA), 2015 IEEE International Conference on*. IEEE, 2015, pp. 2256–2263.
- [27] J. Ha, F. C. Park, and P. E. Dupont, "Elastic stability of concentric tube robots subject to external loads," *IEEE Transactions on Biomedical Engineering*, vol. 63, no. 6, pp. 1116–1128, 2016.
- [28] J. Lewis, "Fast normalized cross-correlation," in *Vision interface*, vol. 10, no. 1, 1995, pp. 120–123.